



MENTOR Machine LEarning in optical NeTwORks

A European Industrial Doctorate [EC GA 956713]

D3.4/D11

Experimental demonstration and assessment of control and management plane for ultra-wide band optical networks

Document Details

Title	Experimental demonstration and assessment of control and management plane for ultra-wide band optical networks
Deliverable number	D3.4/D11
Deliverable Type	Report
Work Package	WP3
Deliverable due date	August 31, 2024
Actual date of submission	August 16, 2024
Lead beneficiary	SSSA
Main Authors	L. Zar Khan (SSSA), A. Ben Terki (SSSA), Mariano Devigili (UPC)
Contributor (s)	J. Pedro (INF-P), A. Eira (INF-P), N. Costa (INF-P), A. Napoli (INF-G), N. Sambo (SSSA), Ahmed Triki (Orange)

Project Details

Grant Agreement	956713
Project Acronym	MENTOR
Project Title	Machine LEarning in optical NeTwORks
Call Identifier	H2020-MSCA-ITN-2020
Project Website	https://mentor.astonphotonics.uk
Start of the Project	1 January 2021
Project Duration	48 months

Dissemination level

PU	Public	X
----	--------	---



UNIVERSITAT POLITÈCNICA
DE CATALUNYA
BARCELONATECH



Sant'Anna
School of Advanced Studies – Pisa



EC Funding



This project has received funding from the European Union's Horizon 2020 research and innovation programme under the Marie Skłodowska-Curie grant agreement number 956713

Table of Contents

List of Figures	4
Beneficiaries	4
Industrial Partners.....	4
List of Acronyms.....	4
Executive Summary.....	6
1. Introduction	7
2. Experimental assessment of QoT estimation.....	7
3. NN complexity	10
4. DRL in comparison with SOTA DRL	13
5. Alarm clustering and Root-cause identification	16
6. Failure management assisted by Telemetry	17
6.1. Implementation of streaming telemetry in the lab.....	17
18	
6.2. ML-based models for failure detection:	19
6.3. Current work	19
Conclusion	19
References	19

List of Figures

Fig. 1 A blockdiagram showing the experimental testbed used to emulate a long-haul core optical network. It can be subdivided in three modules: transmitter, transmission link (i.e., contained in the re-circulating loop system) and receiver.	8
Fig. 2 DP-QPSK Transmitter scheme (a) and Homodyne Coherent Receiver scheme (b).	8
Fig. 3 Captures realized with an Optical Spectrum Analyzer (OSA) at the input of the RLS. (a) Optical spectrum of the WDM signal. (b) Power evaluation of the S-band (on the left) and of the C-band channels (on the right) before being launched inside the fiber.	9
Fig. 4 (a) BER Measurements (continuous lines) and Estimations (dotted lines) in function of the propagation distance for the DP-QPSK S and C band channels with the corresponding pre-FEC BER Thresholds (dashed lines). (b) Back-to-back characterization of the transceivers for the S band and the C band signals modulated with dual polarization QPSK modulation format and 28 Gbaud symbol rate.	9

Beneficiaries

Aston Institute Of Photonic Technologies (Lead Beneficiary at Aston University)
 Infinera Germany (Non-recruiting Beneficiary)
 Infinera Portugal (Non-recruiting Beneficiary)
 Sant'Anna School of Advanced Studies
 Technical University of Denmark
 Polytechnic University of Catalonia

Industrial Partners

Telecom Italia Mobile
 Orange Telecom Company

List of Acronyms

AiPT	Aston Institute Of Photonic Technologies
ASE	Amplified spontaneous emission
AST	Aston University
CA	Consortium Agreement
DTU	Technical University of Denmark
EC	European Commission
EID	European Industrial Doctorate
ESR	Early Stage Researcher
FF	First fit
GA	Grant Agreement
GGN	Generalized Gaussian Noise
GSNR	Generalized signal to noise ratio
INF-G	INFINERA Germany (Non-recruiting Beneficiary)
INF-P	INFINERA Portugal (Non-recruiting Beneficiary)
MB	Multi band
MENTOR	Machine LEarning in optical NeTwORks
ORANGE	Orange Telecom Company

DM-16QAM	Polarization multiplexing 16 quadrature amplitude modulation
DM-QPSK	Polarization multiplexing quadrature phase shift keying
QoT	Quality of transmission
RL	Reinforcement learning
RSA	Routing and spectrum assignment
SB	Supervisory Board
SP	Shortest path
ML	Machine Learning
NN	Neural Network
NBI	North Bond Interface
PPO	Proximal Policy Optimizer
SRS	Stimulated Raman Scattering
SDN	Software Defined Networking
SSSA	Sant'Anna School of Advanced Studies
TIM	Telecom Italia Mobile
UPC	Polytechnic University of Catalonia

Executive Summary

This deliverable – by building on the previous WP3 deliverable (D3.3) entitled “Final implementation of control and management plane for ultra-wide band optical networks” – presents the final tests and experiments on the MENTOR control plane assisted by ML. The Generalized Gaussian Noise (GGN) model specifically designed for multi band is here experimentally assessed in a multi-band setup. Then, a comprehensive set of results is shown for Deep-Reinforcement-Learning-based resource allocation in multi-band employing the aforementioned model. Then, failure management is assessed paying attention to the complexity of neural networks, given their huge impact on power consumption. Finally, failure management is implemented at an operator setup, employing devices from different vendors.

1. Introduction

The SDN control plane assisted by ML proposed and investigated by ESRs in the MENTOR project is here finally tested. In the context of MB optical networks, the SDN control plane should be refined or even re-designed. As shown in D3.2 (“Initial implementation including the SDN controller with MB-extensions and the agents”), the resource allocation algorithms should account for physical layer constraints of multi band and the implementation of the GGN model was presented accounting for wideband transmission effects such as Stimulated Raman Scattering (SRS). Reinforcement Learning was adopted for resource allocation. Then, neural networks were exploited for (soft-)failure identification in the context of failure management.

In this deliverable, first, the GGN model is experimentally demonstrated in a multi band setup in lab. Then, the DRL-based RSA exploiting the GGN model is extensively analyzed: DRL can lead to an increase in supported network load. Then, failure identification is demonstrated with low-complex neural networks. Finally, the recent activities and implementations on schemes for failure management are presented at an operator setup. Some of these activities are still on going and results are being collected. Sec. 2 presents the experimental demonstration of the GGN model for multi band. Sec. 3 shows the final results for DRL-based RSA, Sec. 4 the complexity reduction of neural networks for failure management. Sec. 5 and 6 show the ongoing activities at a MENTOR operator in the context of failure management. Finally, Sec. 7 draws the conclusions.

2. Experimental assessment of QoT estimation

Fig. 1 shows the block diagram of the experimental data plane. The transmission sources were operating at approximately 1529 nm and 1549 nm, respectively, and were set at the maximum supported power (14 dBm) in order to have a proper launch power at the fiber input (e.g., around -2 dBm), despite the undergone system losses before reaching the re-circulating loop system (RLS).

The two channels are modulated using separate nested Mach-Zehnder modulators (MZM)s. Both these external IQ modulators received the same information signal – a N=11 pseudo random bit sequence (PRBS) with 28-Gbaud symbol rate. The DAC was used to periodically output pulse shaped electrical signals which drove the MZM based IQ-modulators. Dual polarization quadrature phase shift keying (DP-QPSK) signal was achieved. DP was obtained by splitting the signal into two orthogonal polarizations that were de-correlated by delaying them with respect to each other and finally combined by a polarization beam combiner (PBC) as shown in Fig. 2. The S band signal had a ~ 9 dBm total power at the output of the transmitter. This power was reduced to ~ 7 dBm after the filtering of the ASE noise through a band pass filter (BPF). The C band resulted to have a power of ~ 2 dBm. A booster Erbium-doped-fiber amplifier (EDFA) was exploited to set approximately the same launch power over the two distinct channels. The two modulated signals were multiplexed on the same fiber by a 2x1 coupler with a split ratio of 90:10 selected to preserve the power for the more critical S-band channel.

Thus, the coupler input carrying the 90% of the power was assigned to the S band channel, while the 10% input to the C band channel in order to give a higher power to the S band channel. A long-haul transmission line was emulated through a RLS loaded with a ~ 10 dBm wavelength division multiplexing (WDM) signal through the acousto-optic modulator (AOM2), whose insertion loss was 4 dB, and a 2x2 coupler with a splitting ratio of 50:50. Fig. 3 (a) shows the optical spectrum at the RLS input. Among the two channels, the spectral shape of ASE noise can be seen clearly. This relatively high noise was generated by the amplifiers integrated in the transmitter and by the noisy C band booster amplifier. At each circulation, the WDM signal was propagated along a 40 km SMF. The S band and C band channels entered in the fiber with a launch power of -3.0 dBm and -2.3 dBm as shown in Fig. 3 (b) and as expected they experienced different fiber losses of 8.5 dB and 7.9 dB, respectively. The re-

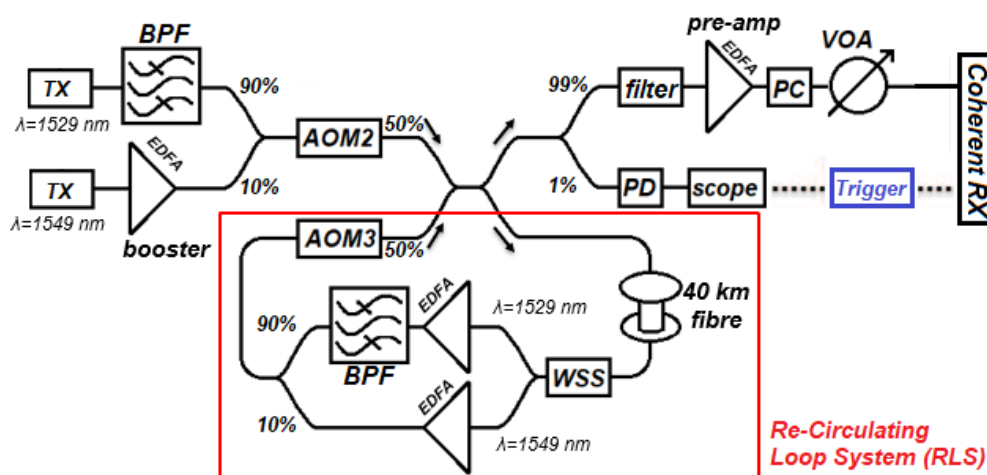


Fig. 1 A blockdiagram showing the experimental testbed used to emulate a long-haul core optical network. It can be subdivided in three modules: transmitter, transmission link (i.e., contained in the re-circulating loop system) and receiver.

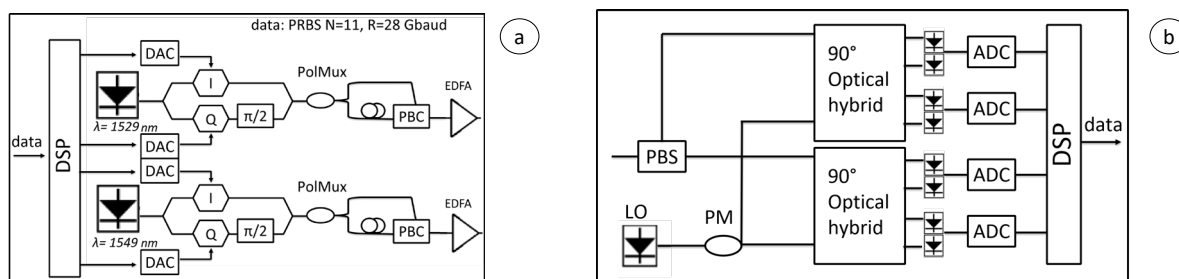


Fig. 2 DP-QPSK Transmitter scheme (a) and Homodyne Coherent Receiver scheme (b).

circulating loop includes also a wavelength selective switch (WSS) operating in the range of 191.250–196.275 THz which allowed to switch the C and S-band signals over two different output ports in order to enable a dedicated amplification per band. At the end of the loop, AOM3 was used to enable re-circulation through 2x2 input port, or to empty the system after each run. At the loop output, a 1x2 splitter (99:1) sends most of the power to the coherent receiver for data recovery and performance estimation. A small amount of power is finally provided to an oscilloscope after opto-electronic conversion for loop synchronization (i.e., selecting the proper propagation distance) and receiver triggering.

At the receiver side, a pre-amplifier was employed in order to compensate the losses introduced by the RLS and by the filter. Moreover, before the receiver, a polarization controller (PC) and a variable optical attenuator (VOA) were included to align the I-Q signal polarizations and to control received power, respectively. In the coherent homodyne detector, the optical signal was demodulated employing the polarization-and phase-diversity technique. After a polarization beam splitter (PBS), the received QPSK signals were mixed with the LO through a 90° optical hybrid, whose outputs were sent to four couples of balanced photo-diodes (see Fig. 2). The four photo-detected signals were sampled and digitised through a real-time oscilloscope. The sampled signals were saved or offline digital signal processing (DSP). Finally, symbol decisions were made and the BER was computed. The BER was evaluated on a number of cycles higher than 100 after which possible to detect minimum BER values in the order of 10⁶.

Fig. 4 (a) shows the measured BER in logarithmic scale of the transmitted channels as a function of the distance reached by the S band and C band channels. For the C band, the FEC threshold (i.e., the maximum bit error rate

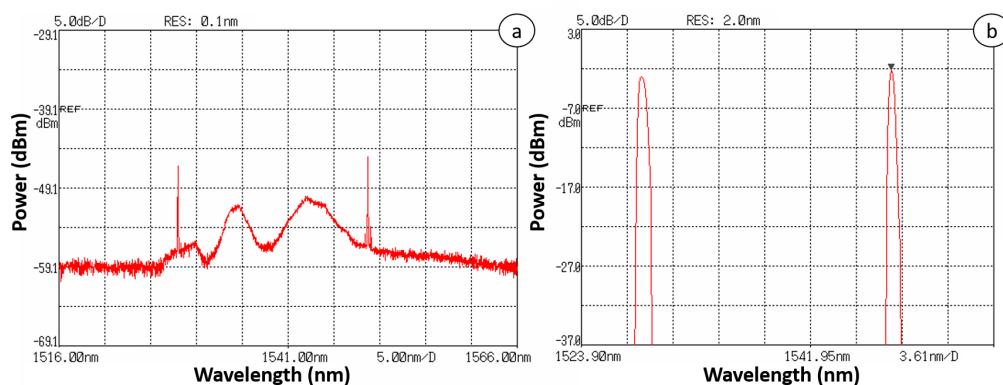


Fig. 3 Captures realized with an Optical Spectrum Analyzer (OSA) at the input of the RLS. (a) Optical spectrum of the WDM signal. (b) Power evaluation of the S-band (on the left) and of the C-band channels (on the right) before being launched inside the fiber.

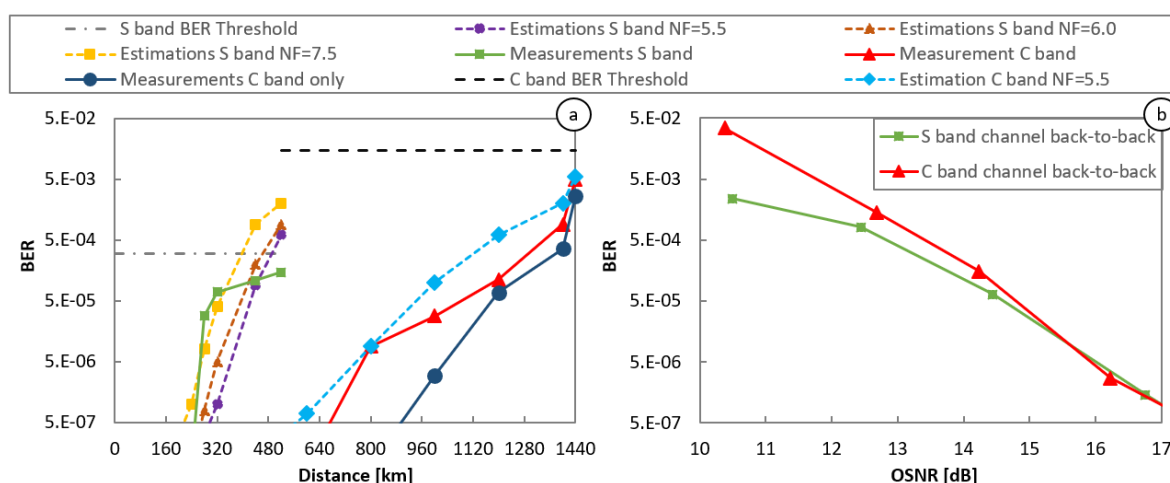


Fig. 4 (a) BER Measurements (continuous lines) and Estimations (dotted lines) in function of the propagation distance for the DP-QPSK S and C band channels with the corresponding pre-FEC BER Thresholds (dashed lines). (b) Back-to-back characterization of the transceivers for the S band and the C band signals modulated with dual polarization QPSK modulation format and 28 Gbaud symbol rate.

that allows to recover data) was set to 1.5×10^{-2} whereas for the S band the considered FEC threshold was 3×10^{-4} . The experimental testbed aims at emulating a lightpath of a long-haul optical network where the transmission line is composed by 40 km links and the in-line amplification is performed by two distinct EDFAs, each one dedicated to a specific band. The system power losses introduced jointly by the AOM3 and by the 2x2 coupler (≈ 7 dB) may be interpreted as insertion losses of a reconfigurable optical add/drop multiplexer (ROADM) in a core optical network with ≈ 16 dB spans.

As expected, the C band channel presented better performance (i.e. a lower BER) when launched alone into the fiber than when multiplexed together with the S band channel, given non-linear impairments induced by the S-band channel (e.g., cross-phase modulation - XPM). However, the XPM and the SRS induced by the S-band channel did not excessively affect the performance of the C band channel, which still reached 1440 km (i.e., 36 spans). Regarding the S band channel, it had a shorter maximum reach of 520 km (i.e., 13 spans) due to its lower launch power, the higher experienced attenuation, and the lower available amplification gain. In addition, the S band channel suffered of cascaded filtering effects induced by the BPF.

Fig. 4 (a) also compares the BER measurements with the BER estimations. The GNPY tool was adapted to the experimental lightpath with some channel-dependent system parameters (e.g., fiber loss, WSS loss, EDFA gain and NF) derived from power measurements computed along the first re-circulating loop. The QoT estimations

in terms of general signal-to-noise ratio (GSNR) were then translated into BER estimations through the TRX/RX characterization in back-to-back shown in Fig. 4 (b) similarly as in [Ne14].

Regarding the C-band channel, the GNP_y estimator provided a conservative QoT estimation, i.e., similar or higher BER compared to the one of the measurements. Thus, if this model was applied in a control plane architecture – where a network controller holds a GNP_y module to verify path feasibility – then the Software Define Networking (SDN) controller would set up a lightpath with acceptable QoT. In other words, the GNP_y module, when asked to estimate the BER for a link having a DP QPSK modulation format, a 28 Gbaud symbol rate would always give a BER value higher than the actual one. For the S band channel, the EDFA's NF was unknown and therefore estimations assuming different NF values were performed as shown in Fig. 4 (a). For short distances, the S band QoT estimation was optimistic. This was due to the unknown NF. However, the estimated BER was lower than the measured one only for values below the pre-FEC BER threshold (e.g., for distances between 200 and 400 km). Conversely, for more critical distances (e.g., larger than 400 km), the GNP_y tool was conservative providing an estimated BER higher than the measured one. Thus, in conclusion, the extended GNP_y tool provides conservative estimations both in S and C bands.

3. NN complexity

The computational complexity of ML solutions investigated for optimizing the operation and performance of optical networks has yet to receive the attention it deserves from the research community. High computational complexity leads to increased energy consumption and operational costs, so it is critical to ensure that ML-based solutions for optical networks have high performance as well as low computational complexity. We proposed an approach in [Khan-ONDM2024] for optimizing neural networks (NNs) used for failure management in optical networks, with failure identification as the use-case. In this report, findings of our aforementioned published paper are presented.

3.1. Proposed Approach to Optimize NNs

We propose, to the best of our knowledge, the first iterative algorithm that optimizes NNs for low computational complexity and memory footprint by monitoring neuron activity during the inference phase. Traditional methods such as grid search, random search, and Bayesian optimization do not rely on neuron activity and thus may not always produce a NN architecture that is optimized for a good balance of predictive performance and computational complexity. These methods typically select the NN size that maximizes accuracy/F1-score or minimizes loss on validation set for a given use-case, without regard for the computational complexity of the NNs used to achieve that high predictive performance. For example, Bayesian optimization, which is commonly used to determine NN size and other hyperparameters, frequently produces an underutilized NN due to many inactive neurons. To demonstrate the inactivity of some hidden layer neurons, we used an experimental dataset (detailed in the following section) for training and testing purposes. We used Bayesian optimization to determine the hyperparameters of a NN-based failure classifier, and the resulting feed-forward NN architecture (NN_{base}) had four hidden layers [h_1, h_2, h_3, h_4] with [290, 30, 117, 233] neurons, respectively, and achieved a macro-averaged F1-score of 0.983 on the test set. The non-linear activation function for these hidden layer neurons was rectified linear unit (ReLU), which activates a neuron only when the weighted sum of its inputs is positive and outputs that positive value. If we examine the trained NN_{base} to see how each neuron contributes to inferences, relative neural activity (RNA) in each hidden layer can be quantified as:

$$RNA = \frac{\sum_{i=1}^N a_{j,k}(X_{test}^i)}{\max_j \sum_{i=1}^N a_{j,k}(X_{test}^i)} \quad (1)$$

Where $a_{j,k}$ represents the output of k^{th} neuron in j^{th} hidden layer, and X_{test}^i represents the i^{th} sample in the test set. Each neuron's activity is normalized relative to the neuron with the highest activity in that layer for the entire test set. Fig. 5 shows the RNA of all hidden layer neurons of the trained NN_{base} , which achieved a 0.983 F1-score on the test set. Many neurons, i.e., [70, 10, 32, 86] in $[h_1, h_2, h_3, h_4]$, have zero RNA score and thus have no contribution in the inference. However, their redundant presence adds unnecessary computational complexity.

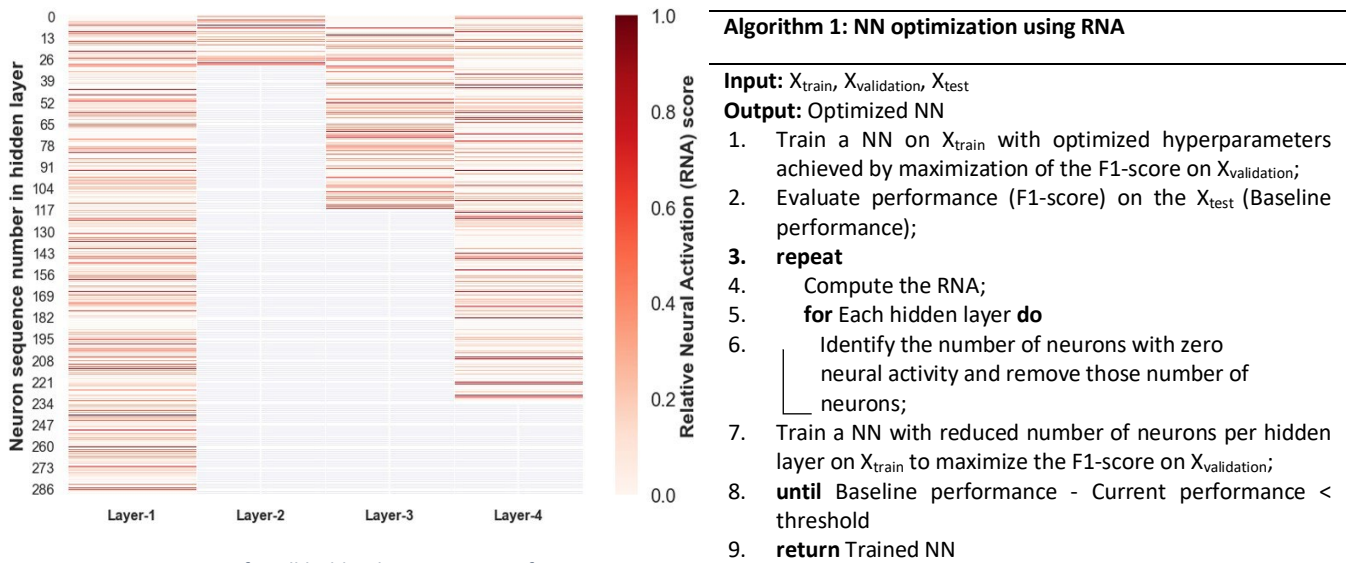


Figure 5: RNA score for all hidden layer neurons of NN_{base}

The proposed algorithm (Algo. 1) relies on the identification and removal of redundant neurons. It takes training, validation, and test sets as input and proceeds as follows: first, it optimizes hyperparameters such as learning rate, batch size, number of hidden layers, and number of neurons in each hidden layer to maximize the F1-score on the validation set. The trained neural network is then evaluated on the test set (*Baseline Performance*). The algorithm then initiates an iterative procedure in which it computes RNA for each hidden layer, identifies the number of neurons with no neural activity, and removes the corresponding number of neurons from each hidden layer. The algorithm then trains a neural network with a reduced number of neurons per hidden layer, as determined in the previous step. It then assesses performance over the test set (*Current Performance*). This iterative process continues until a stopping condition is met. In our work, the stopping condition is met when *Current Performance* decreases by more than a given *threshold* compared to *Baseline Performance*. The algorithm's final output is an optimized NN with lower computational complexity and a smaller memory footprint, with no discernible impact on predictive performance (e.g., F1-score).

3.2. Experimental Validation

3.2.1. Experimental testbed setup for data acquisition

Fig. 6 depicts the experimental testbed used for data collection. The testbed consists of two commercial transponders used as transceivers tuned at 100 Gb/s with DP-QPSK modulation.

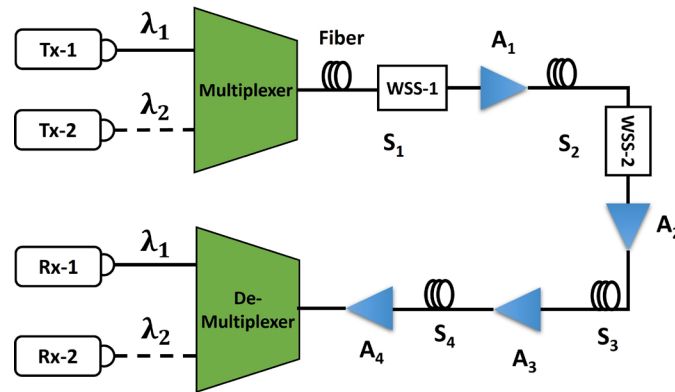


Figure 6: Experimental Testbed Setup

Two channels were set up: λ_1 at 194.1 THz and λ_2 at 194.2 THz, both with a spectral width of approximately 37.5 GHz. For this work, all the performance metrics reported consider λ_1 . Arrayed waveguide gratings were used to multiplex and demultiplex optical channels. The link had four single-mode fiber spans, each 80 km long. Four erbium doped fiber amplifiers (EDFAs) were utilized to compensate for fiber losses. WSSs were placed at the end of span 1 and 2 to simulate failures. The bit error rate (BER) and optical signal-to-noise ratio (OSNR) at the receiver were collected from the testbed every 4 seconds and used as input features for NN. For normal operation, channel-1's central frequency of WSSs was set to 194.1 THz, with 0 dB of extra attenuation and 50 GHz channel bandwidth. This work considered three soft failures: filter shift + attenuation, attenuation, and filter tightening + attenuation.

3.2.2. Results and complexity analysis

We evaluated using a threshold = 0.01 (corresponding to 1% F1-score reduction), resulting in 6 iterations. Tab. 1 shows the results from each iteration. The results show that the number of neurons decreased with each iteration without having a significant impact on the test set's macro-averaged F1-score. Specifically, the number of neurons in some of the hidden layers decreased by up to 86.26%, with minimal impact on the F1-score of 0.01. We quantified the reduction in complexity per iteration using the number of real multiplications (RMs) as a metric. For a dense (i.e., fully connected) layer of a feed-forward NN, RMs can be calculated as $n_i \times n_n$, where n_n is the number of neurons in the layer and n_i is the number of inputs to each neuron in that layer.

Fig. 7(a) depicts the computational complexity per inference in terms of RMs over various iterations. It suggests that removing redundant neurons from the NN's hidden layers can significantly reduce computational complexity. In this case, we reduced the number of RMs by 96.31%, which is a significant gain with minimal impact on NN's predictive performance for failure identification. We also used memory footprint as a metric to calculate how much memory is required to store/deploy the resultant NN at each iteration. Fig. 7(b) shows that the memory footprint is reduced by 87.12%, following a similar trend to that of RMs.

Table 1: NN size and corresponding F1-score after each iteration

Iteration	Hidden layers' neurons [h1, h2, h3, h4]	Macro-averaged F1-score
NN_{base}	[290, 30, 117, 233]	0.983
1	[220, 20, 85, 147]	0.982
2	[162, 16, 61, 93]	0.982
3	[119, 11, 46, 68]	0.981
4	[91, 8, 30, 39]	0.977
5	[65, 7, 21, 32]	0.973
6	[52, 6, 15, 19]	0.967

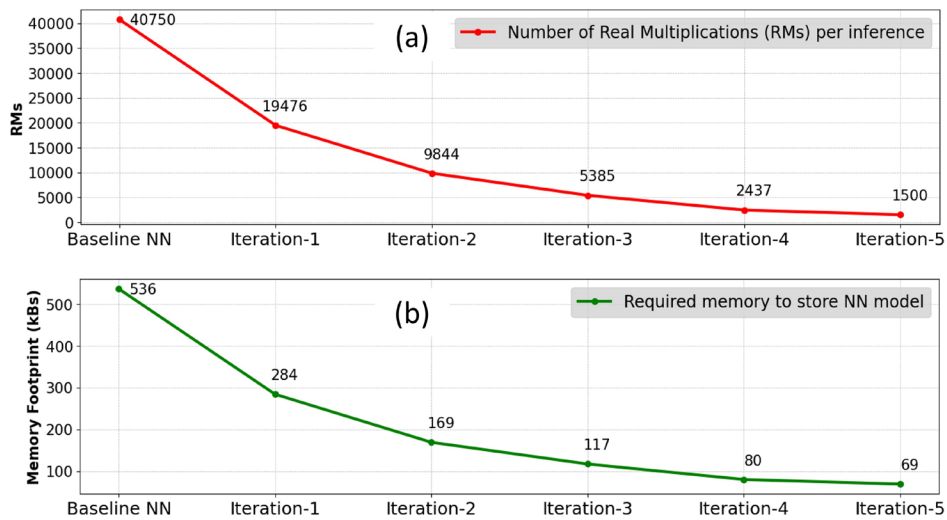


Figure 7: a) Computational complexity in terms of RMs, (b) Memory footprint after each iteration

4. DRL in comparison with SOTA DRL

Multi-band (MB) optical networks extend the lifespan of existing fiber infrastructures by exploiting unused spectrum portions. Simultaneously, Machine Learning (ML) techniques, including Reinforcement Learning (RL) and Deep Reinforcement Learning (DRL), are increasingly used for optimizing optical networks, particularly for routing and spectrum assignment (RSA) and failure management. In our recent study, we proposed RSA strategies based on RL and DRL for multi-band optical networks, as detailed in [Author-2024]. This report presents the findings of our published work, focusing on the optimization of routing and spectrum assignment in optical networks.

4.1. DRL for Multi-Band Optical Networks

We implement an RSA strategies based on RL and DRL for multi-band optical networks, where channel performance can vary significantly. The Generalized Gaussian Noise (GGN) model [Cantono-JLT2018], which accounts for wide-band transmission impairments like Stimulated Raman Scattering (SRS), is used for accurate physical layer modeling. Simulation results across different network topologies show that RL and DRL-assisted RSA significantly reduce blocking probability and increase network throughput compared to benchmark

heuristic RSA algorithms. DRL uses one or more Deep Neural Networks (DNNs), specifically the policy neural network, to approximate Q-table values from RL. DRL training occurs offline, decoupled from its online implementation. The DNN generates a probability distribution of actions, similar to RL scores, and actions (path, channel) are selected based on this distribution. This work implements a DRL environment based on the Gym-Optical-RL toolkit [Natalino-ICTON2020], considering GSNR with linear, non-linear effects, and SRS using GNPY [Ferrari-JOCN2020]. Proximal Policy Optimization (PPO) is chosen as the DRL agent. In this extended version of previous work [BenTerki-PSC2023], we introduce a new DRL-based RSA for multi-band networks and provide additional details and results. Using the GNPY tool for GSNR calculation, the results demonstrate that both RL and DRL-assisted RSA can reduce blocking probability by up to 50% compared to K-Shortest Path and First Fit (K-SP FF) strategies, increasing network load capacity. Specifically, for a blocking probability of 2×10^{-2} , RL-RSA increases load by 20% (250 to 300 Erlang), and DRL-RSA by 80% (250 to 450 Erlang). However, at low traffic loads, simpler RSA techniques may suffice as DRL's benefits diminish. Simulation results also indicate that the C band is the most used, followed by L, S, and E bands, matching the distribution of channels' GSNR values. At very low traffic loads, RL outperforms DRL in reducing blocking probability but requires more transmitter/receiver interfaces due to DRL's dependence on a large training dataset. At medium and high traffic loads, DRL achieves lower blocking probability and uses fewer interfaces than both RL and heuristic strategies. The reward function is action-dependent, and the tuned hyperparameters are detailed in Table 2.

Table 2: DRL Hyperparameters.

DRL Hyperparameter	Value
Learning Rate (α)	5.32×10^{-4}
Discount Factor (γ)	9.86×10^{-1}
Clip Range	1.64×10^{-1}
Entropy Coefficient	2.82×10^{-4}
Total Number of Steps	480000
Policy Optimizer	PPO
Training Time [Hours]	23 (400 Erlangs)

4.2. Evaluation of RSA Strategies

The proposed RSA strategies for MB optical networks are compared with two benchmarks: (i) a load balancing strategy using K-shortest paths (K-SP) for path computation and First Fit (FF) for spectrum assignment, and (ii) a state-of-the-art (SoTA) DRL strategy with GSNR estimated using GNPY and a reward function of +1 for a successful (path, channel) establishment and -1 otherwise. The RSA strategies are analyzed through simulations using various network topologies. The Japanese network topology, consisting of 14 nodes and 44 links, was considered. Traffic follows a Poisson distribution with rate λ , and connection holding time is exponentially distributed with an average of 1 hour. Traffic load (λ/μ) is varied with λ . We assume 400 Gb/s requests, which can be served via a single DP-16QAM channel in 75 GHz or 2×200 Gb/s DP-QPSK channels over 150 GHz. GSNR

is computed per wavelength using GNPY, accounting for SRS. A C-L-S-E band system is assumed, with the supported spectrum and GSNR thresholds of 24 dB for DP-16QAM and 16 dB for DP-QPSK.

Algorithm 2: DRL reward function

Require: $(path, channel) \leftarrow Reward$
 $\alpha \leftarrow \text{Number of allocated channels}$
 $\beta \leftarrow \text{Number of hops in the selected path}$
if the connection can be established **then**
 $Reward \leftarrow 1 + \frac{1}{\alpha \times \beta}$
else if a connection cannot be established on that path and channel **then**
 $Penalty \leftarrow -1$
end if

Algorithm 3: Score update per (path,channel)

Require: $(path, channel) \leftarrow \text{score update}$
if the connection can be established **then**
if one channel with DP-16 QAM modulation format is assigned **then**
 $Reward \leftarrow Q\text{-Table}[state][action] \times 0.75$
else if Two channels with DP-QPSK modulation format are assigned **then**
 $Reward \leftarrow Q\text{-Table}[state][action] \times 0.25$
end if
else if a connection cannot be established on that path and channel **then**
 $Penalty \leftarrow -(Q\text{-Table}[state][action] \times 0.25)$
end if

4.3. Simulation Results

Fig. 8 shows the BP at varying traffic loads in the Japanese topology. RL-RSA achieves the lowest BP for lower traffic load (200 Erlangs) and for medium and higher traffic loads (from 250 to 450 Erlangs) the DRL-RSA achieves lower BP. K-SP FF, which performs load balancing, achieves better performance than RL-Routing, whose routing algorithm is mainly based on distance. RL-RSA and DRL-RSA significantly decrease BP. e.g. by half compared to K-SP for a load of 250 and 450 Erlang, respectively. This is because DRL-RSA and RL-RSA dynamically update their network view by altering scores after choosing an action with rewards assigned according to Algorithm 2 and Algorithm 3 in case of RL-RSA and DRL-RSA, respectively. At low loads, RL performs better than DRL since DRL can only exploit a limited training dataset because of the low number of connections at low loads. On the contrary, at medium and higher loads, DRL can exploit a proper training dataset achieving better performance than RL. Comparing the SoTA DRL-RSA strategy to the proposed DRL-RSA strategy which has a new reward function that takes into accounts the assigned resources to each request. It is noticeable that the proposed DRL-RSA outperforms the SoTA DRL-RSA, in terms of BP, significantly at high traffic loads and with less difference at low and medium loads. With DRL-RSA and RL-RSA, the BP reduction reflects in a throughput increase: e.g., for a BP of 2×10^{-2} , the load rises by 20% (from 250 to 300 Erlang) and by 80% (from 250 to 450 Erlang) with respect to K-SP FF with RL-RSA and DRL-RSA, respectively.

Fig. 9 illustrates the total number of transmitter/receiver interfaces used for RL-RSA, K-SP FF and DRL-RSA algorithms. For traffic loads between 250 and 450 Erlang, K-SP FF has a lower usage of interfaces ranging from 25% to 33% and from 22% to 24% compared to both RL-RSA and DRL-RSA, respectively. The higher interface usage with the RL-RSA and DRL-RSA algorithms is due to two reasons: i) RL-RSA and DRL-RSA reduces BP compared to K-SP FF, as shown in Fig. 8, meaning that they successfully route more traffic for the same offered load, thus requiring more interfaces; ii) RL-RSA and DRL-RSA achieve more effective load balancing, which necessitates longer connections and a higher use of the lower-order modulation format (i.e., DP-QPSK), increasing the interface count.

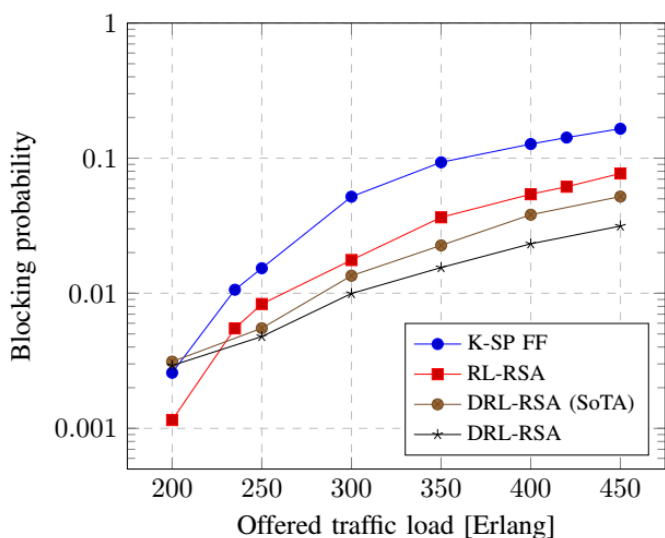


Figure 8: BP versus traffic load in the Japanese topology

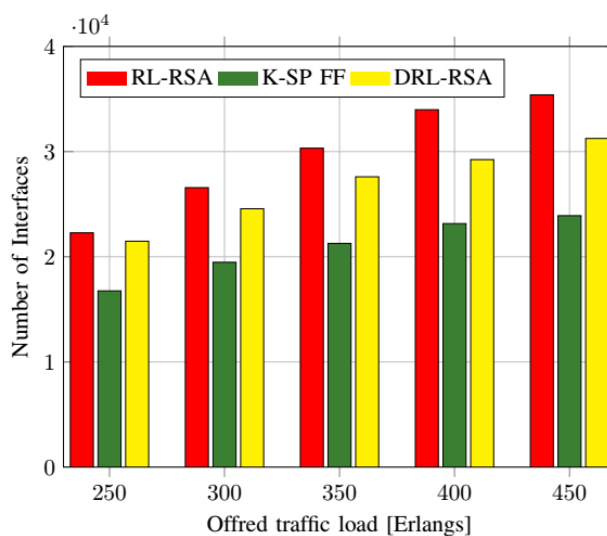


Figure 9: Interfaces usage in the Japanese topology.

5. Alarm clustering and Root-cause identification

An event in a large-scale optical network can trigger a flood of alarms in the Network Management System (NMS). Efficient alarm clustering, followed by root-cause identification, is crucial for timely fault rectification. Alarm clustering simplifies the alarms’ analysis by grouping related ones together. This allows operational teams to focus on resolving the root cause faster than dealing with individual alarms. Using the clusters obtained from the clustering framework presented in [Tchofo-ECOC2023], we proposed a root-cause identification framework. The first step is to validate the clusters by determining whether there is any temporal (i.e., in time domain) overlap between clusters within the topology. It is important to validate the accuracy of clusters as authors in [Tchofo-ECOC2023] achieved clustering using unsupervised ML algorithms like K-means clustering where “K” i.e., number of clusters is determined using elbow method which may not necessarily be always optimal. Therefore, an additional stage of temporal validation can improve the overall alarms clustering.

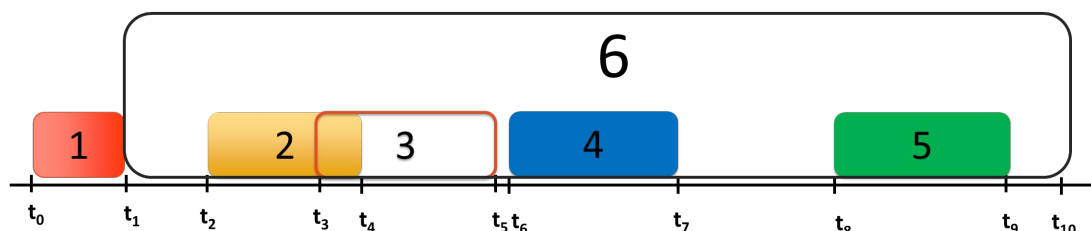


Figure 10: Temporal Validation of Clusters

Fig. 10 depicts how we attempt to validate clusters temporally. For example, clusters 1 and 5 neither have an overlap nor they are temporally close as determined by a pre-specified threshold, therefore we can consider them as valid. On the other hand, clusters 2, 3, and 4 may correspond to the same failure event as clusters 2 and 3 have a temporal overlap, and clusters 3 and 4 are relatively close, so we may need to merge these clusters. Cluster 6 is highly likely to be invalid because it has a much longer period (i.e., the time difference between the earliest and latest alarm within a given cluster) than the other clusters.

After validation of clusters, we determine the correlation between the clusters based on affected network object (e.g., transponder, amplifier, WSS etc.) and native probable cause provided by NMS. The correlation is calculated using a similarity metric known as the Jaccard similarity coefficient, which is a statistic used to assess the similarity and diversity of sample sets. For clusters A and B, Jaccard's similarity can be computed as:

$$J(A, B) = \frac{|A \cap B|}{|A \cup B|} \quad (2)$$

where $|A \cap B|$ is the intersection of alarms in both clusters normalized w.r.t $|A \cup B|$ that results in value in the range of $[0,1]$. Based on some pre-specified high threshold (≥ 0.8), we group similar clusters into a bigger family of cluster with each family representing a different root cause.

6. Failure management assisted by Telemetry

Preventive fault detection and localization in optical networks is a recent and complex topic aimed at predicting network failures before they occur [Danshi-ARXIV2022]. These kinds of failures, known as "soft failures," develop a slow degradation of performance due to aging, incompatibility, or component malfunction, potentially leading to complete equipment breakdown over time [Musumeci-JLT2019]. Failure prevention involves monitoring the Quality of Transmission (QoT) and equipment parameters using ML algorithms to predict, identify, and localize potential faults.

Predictive fault detection and localization requires granular data to promptly detect performance degradation. Although North Bond Interfaces of the network management system (NMS) can be used to extract performance-related data, vendors intentionally withhold up-to-date data via NBI to encourage additional module purchases. Consequently, data obtained from the NMS are not suitable to address the failure detection use-case. An alternative approach involves employing telemetry systems for direct data acquisition from equipment. However, operational teams typically avoid granting access of third-party software to equipment due to security concerns. In this study, we will overlook these concerns and, as a first step, focus on developing a streaming telemetry software to collect data from the different equipment of the lab. The second step involves the development AI-based algorithm that will use the acquired data to detect and predict failures.

6.1. Implementation of streaming telemetry in the lab

This telemetry work consists of:

Testbed Creation: To replicate a wide range of failure scenarios, as shown in Fig. 11, we designed a testbed compliant with optical engineering standards and optimized for equipment changes. Our testbed includes a Nokia transceiver/receiver compatible with Google's gNMI telemetry protocol. Between these components lies an optical line, providing flexibility for adding and removing equipment as well as easiness of modifying equipment configuration. This line features Ekinops amplifiers controllable via SNMP.

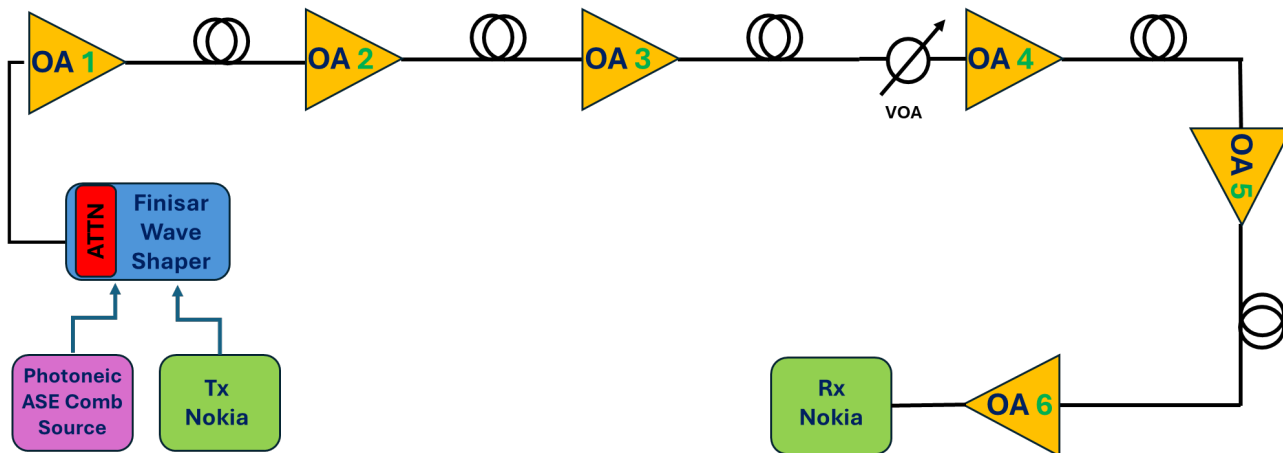


Figure 11: Testbed setup.

Data Collection: We use gNMI and SNMP protocols to extract data from network equipment, as depicted in Fig. 12 . gNMI was chosen for supporting streaming telemetry, enabling continuous metric broadcasting through a subscription system between network equipment and management systems. These features make gNMI more efficient, scalable, and flexible compared to traditional SNMP protocols. While SNMP is less optimized and automated, it remains the only protocol supported on Ekinops equipment. In order to facilitate metric collection, we use the open-source agent “Telegraf “. In our project, Telegraf acts as a connector to gather and store experimental network equipment data into InfluxDB, a real-time database designed for sorting and organizing time-series data, chosen for its open-source nature and specialized functionality. For each failure experiment, we monitor the performance of the optical layer during an interval of 10 minutes. This interval deemed sufficient for capturing gradual equipment degradation. The frequency of extraction is set to 1 minutes in order to ensure an acceptable synchronization between SNMP and gNMI extraction.

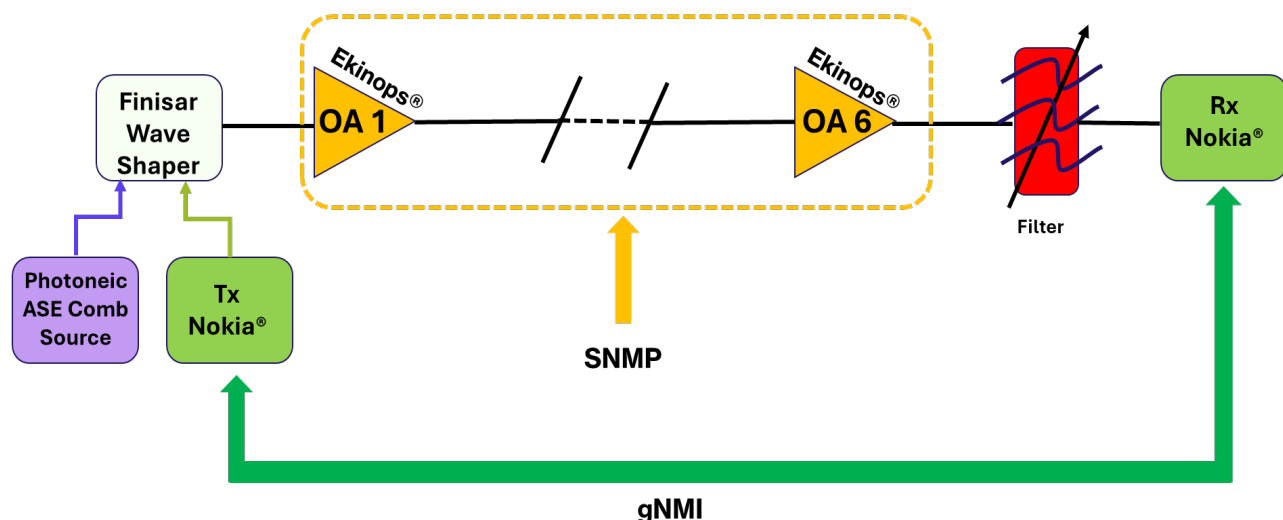


Figure 12: Data collection setup.

6.2. ML-based models for failure detection:

Recent advancements in optical network failure prediction and anomaly detection demonstrate the efficacy of various machine learning techniques. A scheme utilizing Long Short-Term Memory (LSTM) neural networks for adaptive failure prediction includes comprehensive data pre-processing and model training steps to capture temporal features from multi-sourced data, showing high reliability and improved network availability through ten-fold cross-validation [Zhang-PSC2019]. Another study combines statistical hypothesis testing with an ED-LSTM model to accurately model the evolution of soft failures, achieving up to 8.4% improvement in accuracy over traditional methods and emphasizing the importance of real-time predictions [Behera-ICTON2023]. Additionally, a method focusing on network outage prediction employs Q-factor drops and oversampling techniques to prevent overlooked outages, with the standard deviation of the Q-factor proving critical for accurate event classification and effectiveness validated through real data experiments [Hasegawa-COMPSAC2019].

6.3. Current work

We have completed the testbed setup, Fig. 12, for our optical network failure prediction project. The gNMI and SNMP protocols have been implemented, and data extraction is currently ongoing. We are actively conducting analysis of the extracted data to identify anomalies and localize them in the network, which is essential for training robust ML models. This analysis will justify our choice of appropriate ML models for different failure use cases in optical networks, ensuring that our approach is both effective and tailored to the specific challenges of the optical network environment

Conclusion

This deliverable focused on the final tests and demonstrations of the control plane assisted by ML. The GGN model was experimentally demonstrated in a multi-band testbed showing conservative trends with respect to experimental measurements. DRL-based RSA adopting the aforementioned GGN model can strongly increase the routed traffic in the network. Failure identification process complexity is here reduced by more than 80%. Finally, ongoing activities at a MENTOR operator lab show and face out issues of real networks such as alarm clustering and management. Alarm clustering and management is here implemented, as well as streaming telemetry for failure identification.

References

- [sambo-JLT2020] N. Sambo *et al.*, "Provisioning in Multi-Band Optical Networks," in *Journal of Lightwave Technology*, vol. 38, no. 9, pp. 2598-2605, 1 May1, 2020.
- [MENTOR-D3.2] MENTOR D3.2 deliverable "Initial implementation including the SDN controller with MB-extensions and the agents", 2023.
- [Ne14] A. Nespola, S. Straullu, A. Carena, G. Bosco, R. Cigliutti, V. Curriet al., "GN-Model validation over seven fiber types in uncompensated PM-16QAM Nyquist-WDM Links," *IEEE Photonics Technology Letters*, vol. 26, no. 2, pp. 206–209, 2014
- [Khan-ONDM2024] L. Z. Khan, J. Pedro, O. Ayoub, N. Costa, A. Sgambelluri, L. D. Marinis, A. Napoli, and N. Sambo, "Optimizing Deep Learning-based Failure Management in Optical Networks by Monitoring Relative Neural Activity," in 2024 International Conference on Optical Network Design and Modeling (ONDM), pp. 1–3, 2024.

[Tchofo-ECOC2023] D. Maillot-Tchofo, A. Triki, M. Laye and J. Puentes, "Clustering of live network alarms using unsupervised statistical models," 49th European Conference on Optical Communications (ECOC 2023), Hybrid Conference, Glasgow, UK, 2023, pp. 1246-1249, doi: 10.1049/icp.2023.2517.

[Cantono-JLT2018] M. Cantono et al. On the interplay of nonlinear interference generation with stimulated Raman scattering for QoT estimation. *IEEE / OSA JLT*, 36(15):3131–3141, 2018.

[Natalino-ICTON2020] C. Natalino and P. Monti. The optical rl-gym: An open-source toolkit for applying reinforcement learning in optical networks. In 2020 22nd International Conference on Transparent Optical Networks (ICTON), pages 1–5, 2020.

[Ferrari-JOCN2020] A. Ferrari, M. Filer, K. Balasubramanian, Y. Yin, E. Le Rouzic, J. Kundrat, G. Grammel, G. Galimberti, and V. Curri. GNPpy: an open source application for physical layer aware open optical networks. *Journal of Optical Communications and Networking*, 12(6):C31, jun 2020.

[BenTerki-PSC2022] A. Ben Terki, J. Pedro, A. Eira, A. Napoli, and N. Sambo. Routing and spectrum assignment based on reinforcement learning in multi-band optical networks. In 2023 International Conference on Photonics in Switching and Computing (PSC), pages 1–3, 2023.

[Musumeci-JLT2019] F. Musumeci, C. Rottondi, G. Corani, S. Shahkarami, F. Cugini and M. Tornatore, "A Tutorial on Machine Learning for Failure Management in Optical Networks," in *Journal of Lightwave Technology*, vol. 37, no. 16, pp. 4125-4139, 15 Aug.15, 2019, doi: 10.1109/JLT.2019.2922586.

[Danshi-ARXIV2022] Wang, D., Zhang, C., Chen, W., Yang, H., Zhang, M., Lau, A. P. T. (2022). A Review of Machine Learning-based Failure Management in Optical Networks. arXiv preprint arXiv:2208.10677. Retrieved from <https://arxiv.org/abs/2208.10677>

[Zhang-PSC2019] C. Zhang, M. Wang, M. Zhang, D. Wang, C. Song, L. Guan, and Z. Liu, "Adaptive failure prediction using long short-term memory in optical network," in 2019 24th OptoElectronics and Communications Conference (OECC) and 2019 International Conference on Photonics in Switching and Computing (PSC), (2019), pp. 1–3.

[Behera-ICTON2023] S. Behera, T. Panayiotou, and G. Ellinas, "Machine learning for real-time anomaly detection in optical networks," in 2023 23rd International Conference on Transparent Optical Networks (ICTON), (2023), pp. 1–4.

[Hasegawa-COMPSAC2019] Y. Hasegawa and M. Uchida, "Predicting network outages based on q-drop in optical network," in 2019 IEEE 43rd Annual Computer Software and Applications Conference (COMPSAC), vol. 1 (2019), pp. 258–263

EC Funding



This project has received funding from the European Union's Horizon 2020 research and innovation programme under the Marie Skłodowska-Curie grant agreement number 956713